ROYAL SOCIETY OF CHEMISTRY

EDGE ARTICLE

Check for updates

Charged two-dimensional nanochannels with high ion density enabling ultrafast monovalent and multivalent ion conductivity

Lingjie Zhang,[ab] Yunjia Ling, [ID] [ab] Jianglin Yan,[a] Zhenlei Wang,[ab] Yanhui Miao,[a] Haoyu Bai,[a] Tingting Zhang,[a] Shaoxian Song,[a] Mildred Quintana[b] and Yunliang Zhao [ID] *[ac]

Ion conductors with fast ion transport and reliable stability are highly desired for energy storage and conversion devices. While solid-state ion conductors with high safety and energy density are promising materials for a new generation of electrochemical devices, it remains challenging to achieve high ion conductivity, especially for multivalent ions due to the stronger steric effect and electrostatic interactions. Here, we report the well-ordered charged nanochannels with high ion density, typically fabricated by stacking montmorillonite (MMT) nanosheets, to serve as versatile solid-state ion conductors. Characterization studies and molecular dynamics simulations reveal that the "adaptive" nanochannel height of MMT membranes, combined with Coulomb interaction-induced concerted ion movement and surface-charge-governed ion transport arising from the high-packing-density cations inside the negatively charged nanochannels, jointly suppress the steric effect and strong interactions for various cations. As a result, our MMT nanochannels achieve considerably high conductivity for both monovalent (K^+, Na^+, and Li^+) and multivalent ions (Mg^{2+} and Al^{3+}), ~80 to 210 mS cm^{-1} at 80 °C, higher than that of the corresponding bulk solutions and state-of-the-art ion conductors. This work provides fresh perspectives on fast ion transport in nanoconfined environments, and presents a promising route for developing next-generation ionic devices.
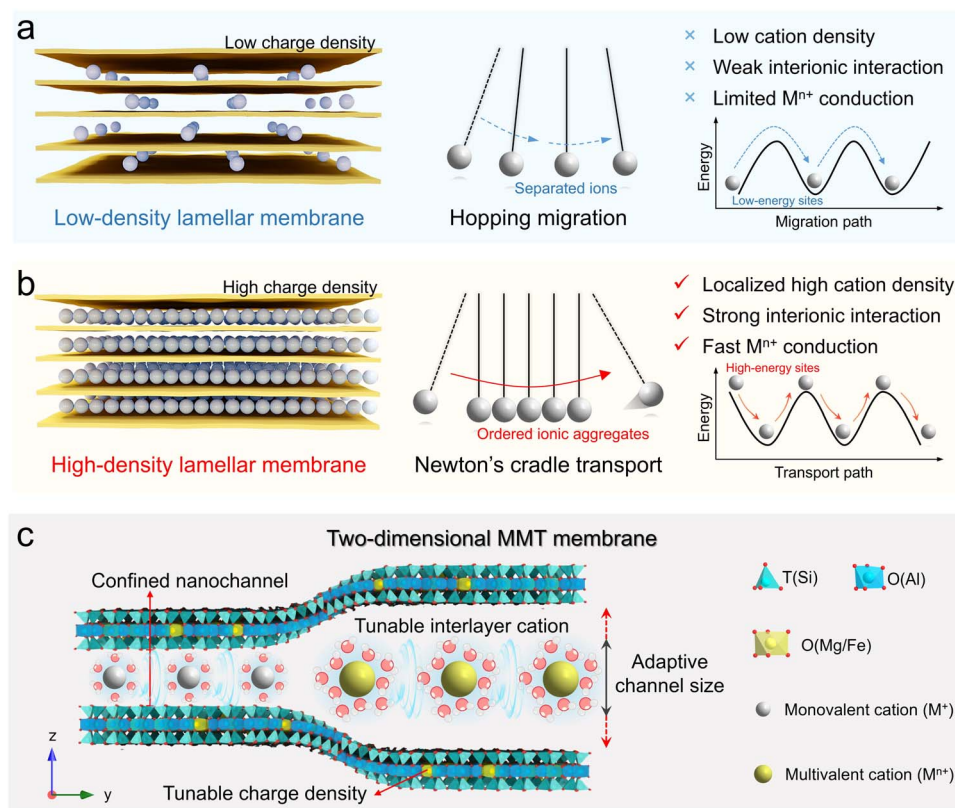
Introduction

The decarbonization and utilization of sustainable energy are driving the development of electrochemical energy storage devices, such as ion batteries, fuel cells, supercapacitors and nanofluidics.[1–4] Ion conductors are the core components that directly determine the performance and lifetime of these devices and are typically expected to rapidly transport charge carrier ions with reliable safety and stability.[5–7] The intrinsic thermal stability and high energy density of solid-state ion conductors render them promising candidates to overcome the limitations of conventional liquid electrolytes.[8–10] Despite notable progress, crucial concerns remain regarding advanced solid-state ion conductors: (i) limited ion conductivity and electrochemical stability, typically 10^{-2} to 1 mS cm^{-1} at room temperature;[11] (ii) poor compatibility with multivalent ions, although multivalent-ion batteries offer higher theoretical

energy densities, lower costs, and sustainable resource availability.[12–14]

Two-dimensional (2D) layered materials with large active surface areas and ordered ion nanochannels offer ideal platforms to construct highways for fast ion transport.[15–21] So far, many 2D lamellar ion conductors have been developed to exhibit high conductivity for monovalent ions (e.g., K^+, Na^+, and Li^+), involving charge-free graphene-based angstrom-scale slits,[22] reduced graphene oxide-based atomic-scale ion transistors,[23] layered metal compounds,[24] and 2D MoS_2 membranes.[25] Nevertheless, the transport behavior of cations in 2D nanochannels is curbed by steric effects caused by ion hydration and electrostatic attraction interaction with the channel walls.[13,26–28] As these effects are strongly dependent on cation valence, the conductivity for multivalent ions in such lamellar ion conductors is typically at least an order of magnitude lower than that for monovalent ions.[22,29]

Given the sandwich microstructures of 2D ion conductors, enhancing channel wall–ion and ion–ion interactions presents two potential pathways toward efficient and versatile ion transport. Nanofluidic studies demonstrate that when electrolytes confined in charged nanochannels with dimensions comparable to the Debye length, ion transport markedly accelerates.[30,31] Accordingly, constructing 2D ion conductors from negatively charged nanosheets appears favorable for facilitating multivalent

[a]School of Resources and Environmental Engineering, Wuhan University of Technology, Wenzhi Street 34, Wuhan, Hubei 430070, China. E-mail: zyl286@whut.edu.cn
[b]Facultad de Ciencias, Universidad Autonoma de San Luis Potosi, Av. Parque Chapultepec 1570, San Luis Potosi 78210, Mexico
[c]Wuhan Clayene Technology Co., Ltd, Tangxunhu North Road 36, Wuhan, Hubei 430223, China

Scheme 1 Schematic of ion conduction in membranes with different charge densities and intrinsic properties of the MMT membrane. (a) Schematic of ion migration in nanoconfined channels with low charge density and its challenges. (b) Schematic of ion transport in nanoconfined channels with high charge density. The high charge density of nanochannels facilitates to create localized high ion density for the formation of ordered ionic aggregates, strengthening interionic interaction *via* Coulomb propulsion and thus accelerating ion conduction. (c) Schematic crystal structures of the MMTs and the unique properties of lamellar MMT membranes.

ion transport. Nevertheless, this introduces low-energy sites with strong electrostatic attraction near negative charges locations to impede ion migration, especially for multivalent cations (Scheme 1a).[12,32] Modulating the interionic interaction between adjacent mobile ions offers another promising solution. In widely studied lamellar ion conductors (*e.g.*, graphene oxide and MXene membranes), however, the nanochannels inherently contain few or no cations, which causes cations to preferentially occupy low-energy sites, encountering high energy barriers to hop between adjacent positions, thus resulting in slow or even suppressed ion transport, especially for multivalent ions (Scheme 1a).[33] We conjecture that constructing high-density cation transport networks within the nanoconfined channels can induce localized packing effects, forcing some cations to gather around the high-energy sites (Scheme 1b). During transport, the downhill migration of these cations can partially compensate for the energy barriers encountered by the following uphill-climbing cations, enabling rapid transport through Coulomb knock-on mechanisms reminiscent of a Newton's cradle.[34,35]

Herein, we demonstrate that leveraging naturally negatively charged montmorillonites (MMTs) as building blocks to assemble into ion-conductive membranes with ordered angstrom-scale channels enables the fast transport of diverse cations. Unlike other 2D nanosheets (*e.g.,* graphene oxide, MXenes, and MoS$_2$),

MMT nanosheets consist of one octahedral alumina sheet sandwiched between two tetrahedral silica sheets. Owing to geochemical isomorphic substitution of Al^{3+} in octahedra by Mg^{2+} and Fe^{2+}, MMT nanosheets exhibit intrinsic negative charge, balanced by exchangeable interlayer cations (Scheme 1c).[36] This natural feature enables tunable charge density, abundant and exchangeable interlayer cations, adaptive channel size and even controllable ion density, highlighting its potential in fabricating intrinsically versatile ion conductors. Consequently, the MMT nanochannel with high charge density and thereby ion density shows universally high ion conductivity for both monovalent (K$^+$, Na$^+$, and Li$^+$) and multivalent ions (Mg^{2+} and Al^{3+}), ranging from ~80 to 210 mS cm^{-1} at 80 °C, substantially outperforming corresponding bulk solutions and advanced solid ionic conductors. Moreover, the developed MMT nanochannels combine long-term durability, exceptional thermal stability, and scalability, offering great promises in diverse ionic devices.

Results and discussion

Preparation of the 2D MMT nanoconfined ion channels

The MMT nanosheets as the building blocks of the nanochannels were prepared by mechanical exfoliation of bulk MMT minerals (Fig. 1a). The resultant dispersions show
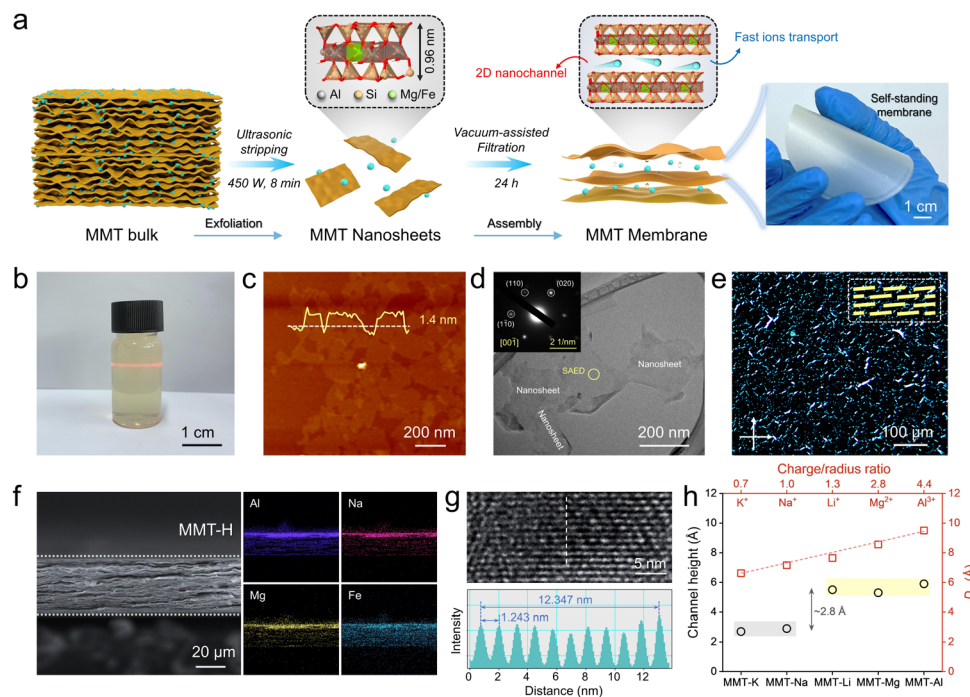
Fig. 1 Fabrication and characterization of MMT nanosheets and assembled nanochannels. (a) Schematic of the fabrication process of MMT membranes. Na–MMT bulks were exfoliated into nanosheets *via* ultrasonic-assisted mechanical stripping, followed by vacuum filtration to obtain the MMT membranes. (b) The photograph of MMT-H nanosheet aqueous dispersion with the Tyndall effect. (c) The AFM image of MMT-H nanosheets, presenting a thickness of about 1.4 nm. (d) The TEM image of MMT-H nanosheets. The inset shows the corresponding SAED pattern. (e) The POM image of MMT-H nanosheet dispersions at 10 wt% concentration. (f) The SEM image and the corresponding EDS elemental mapping of the MMT-H membrane. (g) The HRTEM image of the MMT-H membrane and the corresponding interlayer spacing between adjacent nanosheets. (h) The nanochannel height of MMT membranes and the hydrated diameter of intercalated cations.

a pronounced Tyndall effect, indicating the excellent dispersibility of as-obtained nanosheets (Fig. 1b). The increased isomorphic substitutions of Mg and Fe in high-charge-density MMT nanosheets (MMT-H) causes enhanced negative surface charge compared to low-charge-density MMT nanosheets (MMT-L), along with a visible color shift from white to light yellow (Fig. S1 and S2). Atomic force microscopy (AFM) measurements present that MMT nanosheets are predominantly monolayers with a typical thickness of ~1.4 nm and an average lateral size of ~200 nm (Fig. 1c, S3 and S4). Transmission electron microscopy (TEM) images and the corresponding selected area electron diffraction (SAED) patterns affirm atomically thin nanosheets with monoclinic crystallinity (Fig. 1d and S5). Polarized optical microscopy (POM) images of MMT nanosheet dispersions exhibit bright birefringence stripes, demonstrating the well self-ordering of nanosheets in dispersions, which favors the construction of uniform and ordered 2D channels (Fig. 1e and S6).[37]

Free-standing MMT membranes were readily fabricated by vacuum-assisted assembly of nanosheets due to the self-ordering nature of nanosheets and inherent flexibility of clays (Fig. 1a). Scanning electron microscopy (SEM) images show the uniform and defect-free surface of the assembled membranes (Fig. S7). The cross-sectional images reveal the aligned laminated structures of membranes with uniform distribution of charge-balanced cations and substitutional cations (Fig. 1f and

S8). The results of the energy dispersive X-ray spectroscopy (EDS) prove the markedly higher Mg/Fe substitution degree and thereby interlayer cation amount in the MMT-H membrane (Fig. S9 and Table S1). Notably, MMT membranes illustrate well-defined nanochannels (Fig. 1g and S10). According to small-angle X-ray diffraction (SAXRD) patterns, the interlayer spacing (d) of MMT membranes is ~1.25 nm (Fig. S11), in accordance with the high-resolution TEM (HRTEM) results, indicating the interplanar channels with a height of 0.29 nm after subtracting the single aluminosilicate layer of 0.96 nm.[38] Such nanochannels facilitate the formation of ion transport networks to accelerate the ion conduction.[39] It is noteworthy that the increase in charge density of MMT has not extended the channel dimension, which is attributed to the fact that the interlayer cations also increase, resulting in stronger sheet–ion–sheet attraction interactions.[40]

The nanoconfined channels with other cations can be obtained for versatile ion conductors *via* ion exchange, that is, immersion of MMT membranes into saturated solutions of the desired cation (including K^+, Li^+, Mg^{2+}, and Al^{3+}) for 24 h to replace Na^+ (Fig. S12). Notably, the height of MMT channels does not scale linearly with the hydrated diameter of intercalated cations (D_H), but falls into two distinct values: ~2.8 Å or ~5.6 Å, corresponding to one or two layers of H_2O molecules (Fig. 1h). This suggests that spacing is governed by the formation of mono- or bilayer hydration shells around intercalated

cations. Such behavior correlates with the empirical charge-to-radius ratio (e/r): when $e/r \leq 1$ (low-charge, large ions), mono-layer H_2O forms; when $e/r > 1$ (high-charge, small ions), bilayer H_2O is stabilized, which helps screen electrostatic attraction with channel walls.[14] Such "adaptive" channel height feature minimizes both steric and electrostatic effects, promoting multivalent ion transport. Moreover, the thickness of membranes can be controlled by varying the concentration and volume of the dispersion employed for vacuum-assisted filtration (Fig. S13).

Constructing high-density ion transport networks in MMT nanochannels

Utilizing the typical alkylammonium method (for details, see Text S2),[41] the charge densities of MMT-L and MMT-H membranes were measured to be 0.343 and 0.448 eq FU^{-1} (Fig. 2a), which is consistent with the results of surface potential (Fig. S2), suggesting that the larger the MMT charge density, the more negative the surface charge. The electrostatic potential (ESP) distribution further affirms the charge characteristic of MMT units (Fig. S14), which enables the formation of the surface-charged regions for enhancing ion conductivity.[25] To trace the ion transport networks in nanochannels varying with

the charge density of MMT, we first determined the ion exchange capacity of MMT-L and MMT-H membranes, which is 0.72 and 0.94 mmol g^{-1}, respectively (Fig. S15). Furthermore, the ion densities in nanochannels were calculated after stabilization at 98% relative humidity (RH) (for details, see Text S4). As shown in Fig. 2b, the MMT-H membrane with high charge density presents a significantly higher ion density of ~2 mmol cm^{-3} than the MMT-L membrane. Such high ion density in atomically scale channels facilitates the formation of aligned and high-density packed ionic aggregates, which creates strong Coulomb knock-on interactions among adjacent ions to enable partial occupation of high-energy sites for concerted and fast transport of multiple ions.[24,34] To quantitatively evaluate the ionic aggregation behavior and interionic interaction, we calculated the radial distribution function (RDF) and the corresponding coordination number (CN) of Na^+ in the MMT nanochannels using molecular dynamics (MD) simulations. As shown in Fig. 2c, both MMT-L and MMT-H membranes exhibit first Na–Na characteristic peak at $r = 3.67$ Å, while the density probability (g(Na–Na)) of MMT-H is about three times higher than MMT-L, and similarly appears in the second Na–Na characteristic peak at $r = 5.05$ Å, which demonstrates the reinforced aggregation and interaction of Na^+ in MMT-H nanochannels.[42]
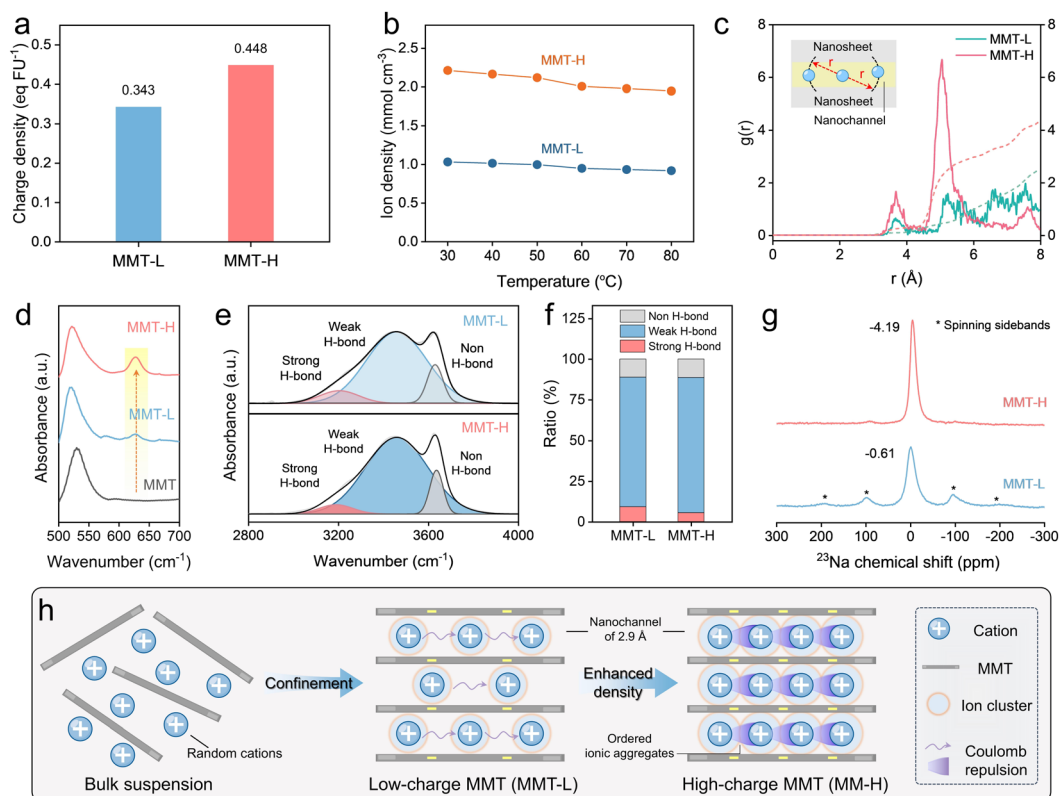

Fig. 2 Experimental and theoretical validation of high-density ion transport networks in MMT nanochannels. (a) The charge density of MMT-L and MMT-H membranes. (b) The ion density within MMT-L and MMT-H nanochannels at 98% RH and different temperatures. (c) RDF curves and the corresponding CN of Na^+ of MMT-L and MMT-H membranes. The inset shows the schematic of the adjacent Na atoms and radius r. (d) FTIR spectra of the MMT nanosheet dispersion, MMT-L membrane, and MMT-H membrane. (e) The fitted O–H stretching vibration of FTIR spectra representing water molecules with strong, weak and non H-bonds in MMT-L and MMT-H membranes and (f) the corresponding proportion. (g) ^{23}Na MAS NMR spectra of MMT-L and MMT-H membranes. (h) Schematic of ion transport and interionic interaction within MMT-L and MMT-H membranes.

This is also proved by the results of CN (represents the average number of adjacent Na atoms).

Fourier transform infrared (FTIR) spectra were used to provide experimental proof of the high-density ion transport networks within MMT nanochannels. As for the MMT nanosheet dispersion, the Si–O–Al bending vibration band appears at 529 cm^{-1},[43] which is red-shifted to 523 cm^{-1} when the nanochannels are formed, unveiling the sheet-ion-sheet attraction interactions within MMT nanochannels (Fig. 2d). Notably, an additional peak is observed at 627 cm^{-1} in MMT-L and is more pronounced in MMT-H membranes, which can ascribe to the ordered and high-density Na$^+$ aggregate networks within the nanochannels.[17,44] Moreover, considering the high-density cations confined in the nanochannels containing 1–2-layer water, we hypothesize that the coordination of water molecules with Na$^+$ disrupts the hydrogen-bond (H-bond) interactions between water molecules.[45] As shown in Fig. 2e, the O–H stretching vibration of water molecules (3000–3800 cm^{-1}) exhibits a typical wide peak convoled into three components corresponding to water molecules with strong ($\sim$3200 cm^{-1}), weak ($\sim$3400 cm^{-1}) and non H-bonds ($\sim$3600 cm^{-1}), respectively.[46] Furthermore, the ratios are determined according to the area of fitted peaks to quantify the H-bond states. With the charge density increasing, the strong H-bond reduces while the weak and non H-bonds increase, reconfirming the high-density cation networks in MMT-H nanochannels (Fig. 2f). The results are supported by Raman spectra as well (Fig. S16). ^{23}Na magic angle spinning nuclear magnetic resonance (MAS-NMR) was also used as a sensitive indicator to investigate ion transport behavior in MMT nanochannels. The ^{23}Na MAS-NMR spectrum of MMT-L membrane shows a strong resonance at −0.61 ppm with multiple spinning sidebands (Fig. 2g). Such a dominant and sharp ^{23}Na signal is attributed to the active Na$^+$ with high mobility in nanochannels.[47,48] As for MMT-H membrane , the ^{23}Na signal shifts to the upfield, suggesting the increased electron density and enhanced interionic Coulomb interaction of Na$^+$.[49,50] In addition, the intensified signal but reduced full width at half-maximum (FWHM) in the ^{23}Na MAS-NMR spectrum of MMT-H with almost disappeared spinning sidebands, also confirms the enhanced Na$^+$ diffusion.[50] Also, the MMT-H membrane presents a larger specific surface area pore size and peak pore size than that of MMT-L (Fig. S17 and Table S2), suggesting that the high charge density might effectively tune the stacking of the MMT layers to provide more ion transport pathways, facilitating ion mobility.[51] Overall, the confinement of random ions within charged nanochannels accelerates ion conduction via offering ordered transport networks, and high-density ionic aggregate networks can be constructed by increasing charge density of building blocks, which induces strong Coulomb interaction between adjacent ions to enhance ion mobility (Fig. 2h).

Ion transport behaviors in MMT nanochannels

To investigate the effect of nanoconfined channels on ion transport, Na$^+$ conductivities in the MMT membranes and bulk solutions with 0.1 or 1.0 M NaCl were first determined. Generally, liquid ion conductors present high conductivity, but obviously depend on temperatures and concentrations. As shown in Fig. 3a, aqueous NaCl exhibits an ion conductivity of 7.95 mS cm^{-1} at 0.1 M, and the value increases to 28.5 mS cm^{-1} at a higher concentration of up to 1.0 M. In contrast, the MMT-L membrane shows a conductivity comparable to that of high-concentration NaCl, indicating that charged nanochannels facilitate ion conductivity. To speak of, the conductivity of the MMT-H membrane is as high as 70.35 mS cm^{-1}, providing a solid proof on the positive influence of high-density ion transport networks.

We then measured the temperature-dependent Na$^+$ conductivity of MMT membranes at 98% RH with two-electrode alternating current impedance. The Nyquist impedance plots present semicircles and spikes in the high and low frequency regions, respectively, demonstrating the purely ion-conducting properties of MMT membranes (Fig. S18).[10] Across the entire tested temperature range, the Na$^+$ conductivity of MMT-H is much higher than MMT-L (Fig. 3b). Notably, the MMT-H membrane exhibits superior conductivity of 151.87 mS cm^{-1} at a temperature of 80 °C. We further calculated the activation energy (E_a) for Na$^+$ transport based on the Arrhenius plots (Fig. 3c). As expected, the MMT-H shows a lower E_a of 12.76 kJ mol^{-1} than MMT-L (20.81 kJ mol^{-1}), suggesting the improved cation kinetic conduction within high-density ion transport nanochannels. This is also affirmed by the conductivity in different humidities (Fig. S19). Moreover, to validate the impact of the charge density of nanochannels, a medium-charge-density membrane (MMT-M) was prepared using nanosheets with the medium Mg/Fe substitution amount, and conductivities were measured (Fig. S20–S22). Accordingly, along with the increased substitution degree and thereby charge density, the conductivity of MMT membranes rapidly grows (Fig. 3d). These results illustrate that adjusting the isomorphic substitution can tune the charge density of MMTs, which modulates the ion density and interionic interaction within assembled nanochannels for fast ion transport.

We further measured the ionic transference numbers (t_{ion}) of MMT membranes via the concentration-driven electrodialysis diffusion (as illustrated in the inset of Fig. 3e). The open-cell voltages of both MMT-L and MMT-H were negative, certifying the negatively charged nanochannels (Fig. 3e).[52] Based on the Nernst equation, the calculated t_{ion} of the MMT-L and MMT-H membranes are 0.764 and 0.829, respectively, suggesting that MMT membranes are Na$^+$ conductors (Fig. S23).[53] Furthermore, the effect of ion species on the ionic conduction was explored to evaluate the universality of MMT membranes as ion conductors. As shown in Fig. 3f, all the MMT membranes present considerable high conductivities for monovalent (K$^+$, Na$^+$, and Li$^+$) and multivalent (Mg^{2+} and Al^{3+}) ions, which are higher than the practically useful value (10 mS cm^{-1}). Note that the nanochannel height of MMT membranes is much smaller than the D_H of intercalated cations, thus these cations have to sherd or compress hydration shells as they enter and reside in the nanochannels (Fig. 1h). While monovalent ions with the small D_H show the higher ion conductivities within MMT membranes, the conductivity only presents a slight reduction with the increasing D_H and cation charges due to the "adaptive" channel
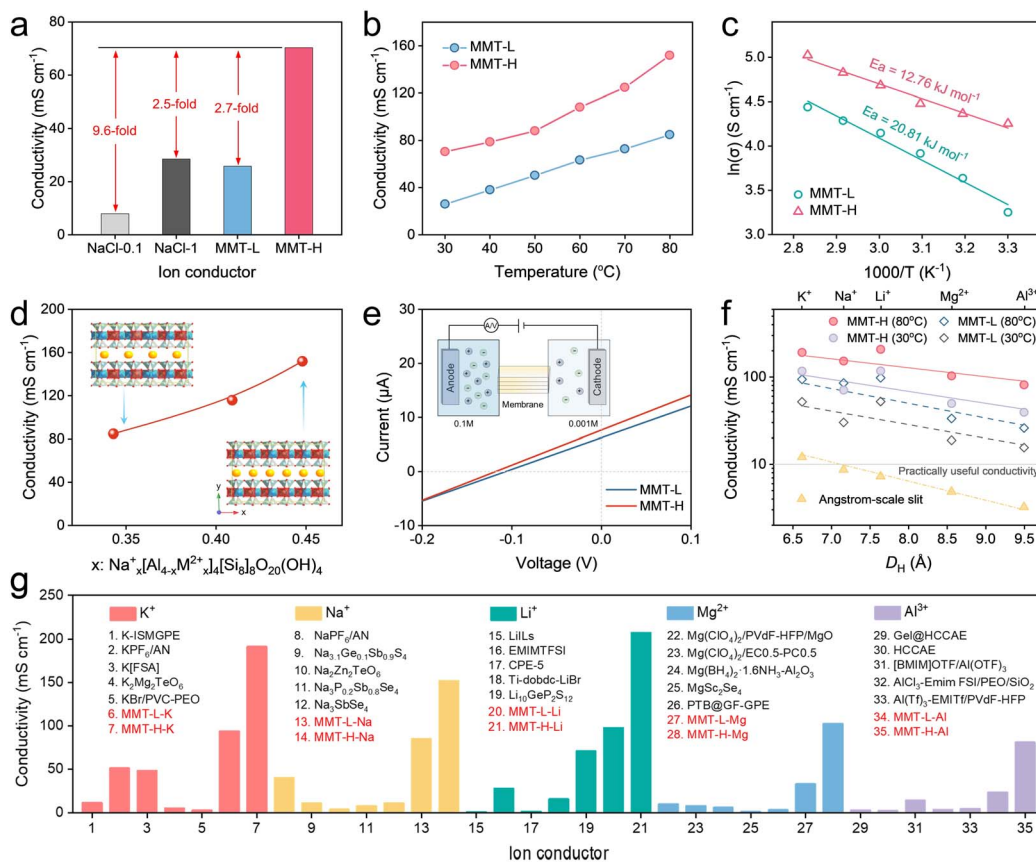
Fig. 3 Cation transport behaviors in MMT nanochannels. (a) The Na^+ conductivity of NaCl bulk solutions (0.1 and 1.0 M), the MMT-L membrane, and the MMT-H membrane. (b) The Na^+ conductivity of MMT-L and MMT-H membranes at 98% RH and different temperatures, and (c) the corresponding Arrhenius plots. (d) The Na^+ conductivity of MMT membranes fabricated by MMT nanosheets with different substitution degrees. (e) The current–voltage curves of MMT-L and MMT-H membranes in a NaCl solution with a 100 times difference in concentration (0.1 M : 0.001 M). The inset shows the schematic of the experimental setup. (f) Conductivities of MMT membranes and the angstrom-scale slit as a function of D_H of cations at 30/80 °C and 98% RH. Dashed curves are guides for the eye, and the practically useful conductivity is presented for comparison. (g) The conductivity comparison between the existing ion conductors and MMT membranes (for details, see Tables S3–S7).

height feature of MMT membranes. In particular, MMT-H membranes still have excellent conductivities over 42 and 80 mS cm^{-1} at 30 and 80 °C for Mg^{2+} and Al^{3+}, respectively. By contrast, common ion conductors, even uncharged angstrom-scale slits, have conductivities of multivalent ions more than an order of magnitude greater than those of monovalent ions (as illustrated by the yellow line in Fig. 3f).[22,29] Apparently, the charged nanochannels and inner high-density ions also play conspicuous roles in conquering the steric effect and strong electrostatic interactions with channel walls.

Additionally, a comparative analysis of the existing ion conductors, involving liquid, gel, solid and 2D ion conductors, highlights the significant advances and universality of charged high-density ion nanochannels in MMT membranes for ion transport. As affirmed in Fig. 3g and Tables S3–S7, the cation conductivities of our MMT membranes exceed those of most state-of-the-art ion conductors under identical conditions.

Ion transport mechanisms of MMT nanochannels

To elucidate the ion transport processes and the mechanisms in MMT nanochannels, we first estimated the effective mobility of

cations in the bulk solutions and nanochannels of MMT membranes based on the Nernst–Einstein relationship (eqn (1)) to explore the comprehensive influence from tortuosity and connectivity of transport channel, and spatial proximity of neighboring ionic groups.[12,54]

$$\sigma = F(c_+\mu^+ + c_-\mu^-) \tag{1}$$

where σ is the ion conductivity and F is Faraday's constant; c_+/c_- and μ^+/μ^- refer to the concentration and mobility of cations/anions, respectively. For negatively charged channels, no anions are allowed to enter, thus c_- is 0 in MMT membranes. In contrast, cations and anions can simultaneously migrate along opposite directions in bulk solutions and free-charge nanoslits, generating ionic current. Fig. 4a illustrates that all the mobilities of cations in the MMT nanochannels are higher than those in bulk solutions, emphasizing the function of ordered and connected nanochannels. Owing to the enhanced ionic aggregation and interionic Coulomb interaction, the ion mobility in MMT-H exceeds that in MMT-L. Moreover, MMT membranes show weak D_H- and cation charge-dependent mobilities, which
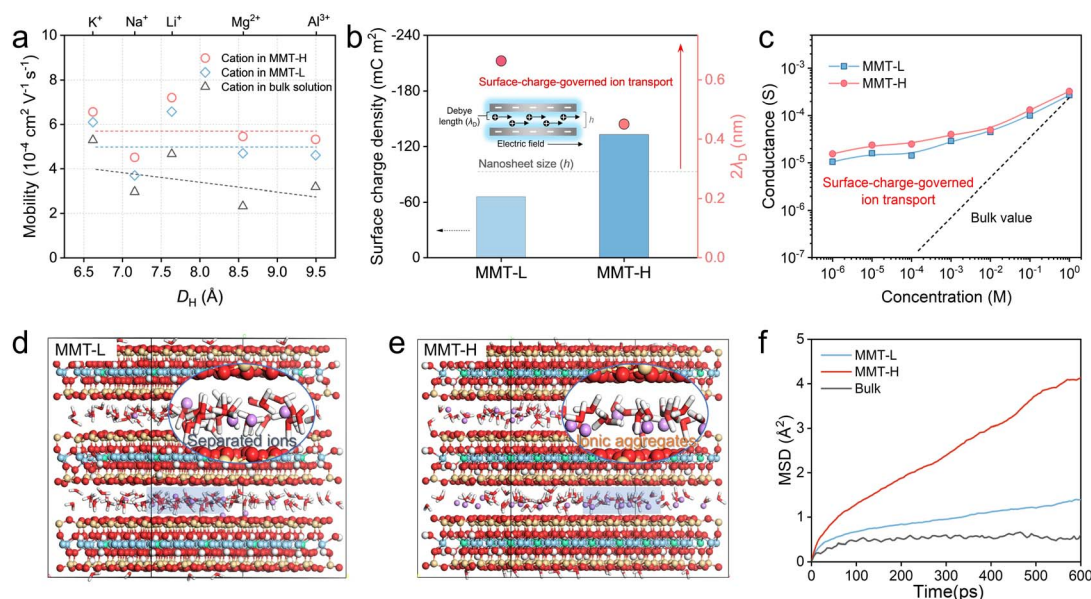
Fig. 4 Cation transport mechanisms in MMT nanochannels. (a) Ion mobilities of MMT membranes and bulk solutions as a function of DH of cations at 30 °C. Dashed curves are guides for the eye. (b) The surface charge density and thickness of the electrical double layer of MMT nanochannels. The inset shows the schematic of the surface-charge-governed ion transport. (c) The conductance of MMT-L and MMT-H membranes as a function of electrolyte concentrations. The optimized equilibrated configuration snapshots of (d) MMT-L and (e) MMT-H membranes in MD solutions. (f) MSD curves of Na⁺ in MMT-L and MMT-H membranes.

is exactly contrary to the reported mobility in free-charge nanoslits,[22] unveiling unique charge-controlled effects.

To explore the effect of the channel charge, we estimated the thickness of the electrical double layer (Debye length, λ_D) of MMT walls based on the Debye–Hückel equation (for details, see Text S5). As displayed in Fig. 4b, the calculated λ_D of MMT-L and MMT-H walls are 0.33 and 0.22 nm, implying that the electrical double layer overlaps in channels with heights of 0.66 and 0.44 nm, respectively, which are higher than the MMT nanochannel size. Accordingly, both MMT nanochannels feature unipolar ion transport governed by surface charge, where conductivity relies on surface charge density (σ_c) of channel walls.[55] Furthermore, we calculated σ_c by using the equation:[56]

$$\sigma_c = \frac{\varepsilon_0 \varepsilon_r \xi}{\lambda_D} \qquad (2)$$

where ε_r and ε_0 are the dielectric constant and vacuum dielectric constant, respectively; ξ is the zeta potential of MMT. The σ_c for MMT-H (-132.99 mC m^{-2}) is twice more than that for MMT-L (-64.61 mC m^{-2}), indicating the enhanced surface-charge-governed ion transport (Fig. 4b). To support our interpretation, we measured the current–voltage (I–V) curves of MMT membranes in NaCl electrolytes using a homemade two electrochemical cell (Fig. S24 and S25). The ion conductance as a function of electrolyte concentrations is summarized in Fig. 4c. The conductance of bulk NaCl solutions shows a linear relationship with the concentration (black dash line). In sharp contrast, the conductance of MMT membranes decreases by only a few tens of times and plateaus at low concentrations as the electrolyte concentration decreases by six orders of magnitude, illustrating typical surface-charge-governed ion transport.

Additional, due to the higher charge density, MMT-H exhibits higher conductance as well.

Given the synergistic effect of the ordered nanochannels, Coulomb interaction-induced multi-ion concerted migration, and the charge-governed transport, the MMT-H membranes perform universal and ultrafast cation conductivity. This is verified by the mean square displacement (MSD) in MD simulations. Fig. 4d and e and S26 show equilibrated configuration snapshots of MMT-L, MMT-H, and bulk solution, which offer insights into the coordination environment and Na⁺ diffusion dynamics. The MSD of Na⁺ was calculated to track kinetic conduction characteristics (Fig. 4f). For MMT-H, the Na⁺ diffusion coefficient is 61.40×10^{-4} Å^2 ps^{-1}, which is 3.84 and 15.31 times that of MMT-L and bulk solution, respectively (Fig. S27), consistent with the experimental results. The results of activation energy barriers for various cations are also in agreement (Fig. S28).

Practicality evaluation of MMT nanochannels

The stability is a common challenge for ion conductors in practical applications. Thus, we comprehensively evaluated the stability of MMT membranes. The hydration of ions is crucial for their rapid transport in channels, while it tends to cause the dimensional swelling, which affects ion conductivity. Fig. S29 and S30 illustrate that the membranes exhibit no noticeable structural change and performance degradation after immersion in NaCl solutions for 48 h, demonstrating their hydrostability. In addition, MMT membranes show anisotropic dimensional swelling with the in-plane swelling <2.55% and through-plane swelling <8.89%, demonstrating the horizontal orientation of the nanochannels (Fig. S31). Compared to the
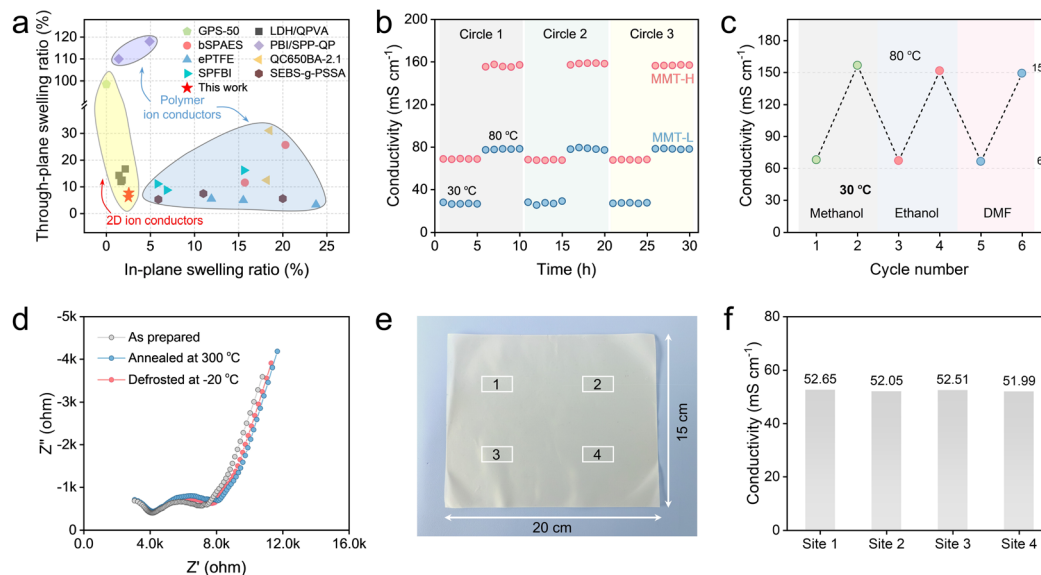
Fig. 5 Conductivity properties of MMT membranes. (a) Dimensional stability of MMT membranes compared with previously reported ion conductors in the literature (for details, see Table S8). (b) Conductivity of the MMT-H membrane after successive heating–cooling cycles and solvent changes. (c) Conducting stability of MMT membranes under three cooling–heating cycles from 30 to 80 °C at 98% RH. (d) Nyquist plots of the MMT-H membrane at 80 °C and 98% RH before and after annealing at 300 °C and defrosting at −20 °C for 12 h. (e) Photograph of a large-scale (300 cm^{-2}) free-standing MMT-H membrane with four randomly selected sites for verification of the uniformity. (f) The conductivity at the four selected sites in *e*.

most polymer and 2D ion conductors, MMT membranes showed excellent dimensional stability, which might result from the aligned interlayer space and sheet–ion–sheet attraction interactions between adjacent MMT nanosheets (Fig. 5a). We further assessed the cycling stability of MMT membranes. Under continuous cooling–heating cycles from 30 to 80 °C (Fig. 5b) and drying–wetting cycles from 30% to 98% RH (Fig. S32), MMT membranes show the unaffected conductivity under each condition, suggesting the long-term durability of MMT membranes resulting from the intrinsic structural stability caused by the close stacking of lamellae.

Moving forward from the intrinsic ion conduction and inorganic nature,[57] the MMT-H membrane also exhibits high stability in organic solvents, where a negligible change in the ion conductivity occurs for the MMT-H membrane after soaking in various solvents (Fig. 5c). As well, the temperature tolerance of the MMT-H membrane was investigated by determining the ion conductivity before and after annealing at 300 °C and defrosting at −20 °C for 12 h at different temperatures (Fig. 5d and S33). The almost overlapping Nyquist plots of impedance data display the excellent thermal and frost durability of MMT membranes, which is difficult to achieve with polymer electrolytes, organic framework-based and even graphene-based ion conductors.

Beyond conductivity, scalability is also critical for practical applications. To evaluate the scale-up potential of MMT nanochannels, a large-area membrane of 20 × 15 cm^2 was prepared by the blade-coating approach. Fig. 5e displays good consistency of the MMT-H membrane during scale-up. Ion conductivity tests at four random selected sites reveal nearly identical values, only slightly lower than that of small membranes

prepared by vacuum-assisted filtration. This indicates that large-scale preparation of MMT membranes can be achieved by designing and optimizing the membrane fabrication process.

Overall, the excellent thermal, solvent, and hydration stability, along with scalability, endows the MMT membrane with enhanced safety, processability and interfacial chemical compatibility for electrochemical device fabrication and optimization, while preventing mechanical and chemical failures, thereby being capable of broadening the electrochemical stability window.[57]

Conclusions

In summary, we develop a versatile solid-state ion conductor by stacking charged MMT nanosheets. By tuning the charge density and intercalated cation, the aligned high-density ion transport networks are constructed in nanochannels of MMT membranes, enabling unexpectedly considerable high ion conductivities for monovalent and multivalent cations, which are hardly realized in conventional ion conductors and even in free-charge nanoslits. It is uncovered that the "adaptive" channel height feature and synergetic contribution of Coulomb interaction-induced concerted ion movement between high-density cations and surface-charge-governed ion transport in charged nanochannels suppress the steric effect and strong electrostatic interactions with channel walls for different cations, thereby facilitating ion conduction. The developed nanochannels also exhibit outstanding conductive, thermal stability, and scalability for practically electrochemical applications. This demonstration not only provides insights into fast ion transport in nanoconfined systems, but also opens

a promising avenue for designing and developing advanced ion conductors for batteries, supercapacitors, and nanofluidic devices.

Author contributions

Lingjie Zhang: Conceptualization, investigation, methodology, data curation, formal analysis, visualization, software, writing–original draft, writing-review & editing. Yunjia Ling: Data curation, methodology. Jianglin Yan: Data curation, formal analysis, investigation. Zhenlei Wang: Investigation, software. Yanhui Miao: Data curation, methodology, software. Haoyu Bai: Conceptualization, validation, writing-review & editing. Tingting Zhang: Project administration, resources. Shaoxian Song: Supervision, resources. Mildred Quintana: Project administration, resources, supervision, validation, writing-review & editing. Yunliang Zhao: Conceptualization, supervision, funding acquisition, resources, project administration, validation, writing-review & editing.

Conflicts of interest

There are no conflicts to declare.

Data availability

Data supporting the findings of this work are presented in the paper and its supplementary information (SI). Supplementary information: additional experimental details and data, including detailed preparation procedures, determination methods, membrane characterization and performance. See DOI: **https://doi.org/10.1039/d5sc08076b**.

All data included in this work are available from the corresponding authors upon request.

Acknowledgements

References

1 H. Zhang, W. Xu, W. Song, K. Peng, L. Sun, C. Yang, X. Zhang, H. Zhang, B. Ye, X. Liang, Z. Yang, L. Wu, X. Ge and T. Xu, *Nat. Sustain.*, 2024, **7**, 910–919.

2 S. Chu and A. Majumdar, *Nature*, 2012, **488**, 294–303.

3 D. Larcher and J. M. Tarascon, *Nat. Chem.*, 2015, **7**, 19–29.

4 L. Zhang, J. Yan, S. Kang, Z. Wang, Y. Miao, R. Gao, T. Zhang, H. J. Ojeda-Galván, M. Quintana, H. Bai, S. Song and Y. Zhao, *ACS Nano*, 2025, **19**, 33620–33631.

5 W. Song, K. Peng, W. Xu, X. Liu, H. Zhang, X. Liang, B. Ye, H. Zhang, Z. Yang, L. Wu, X. Ge and T. Xu, *Nat. Commun.*, 2023, **14**, 2732.

6 A. Manthiram, X. Yu and S. Wang, *Nat. Rev. Mater.*, 2017, **2**, 16103.

7 T. Zhu, Y. Kong, B. Lyu, L. Cao, B. Shi, X. Wang, X. Pang, C. Fan, C. Yang, H. Wu and Z. Jiang, *Nat. Commun.*, 2023, **14**, 5926.

8 Y. Kato, S. Hori, T. Saito, K. Suzuki, M. Hirayama, A. Mitsui, M. Yonemura, H. Iba and R. Kanno, *Nat. Energy*, 2016, **1**, 16030.

9 H. Lian, R. Momen, Y. Xiao, B. Song, X. Hu, F. Zhu, H. Liu, L. Xu, W. Deng, H. Hou, G. Zou and X. Ji, *Adv. Funct. Mater.*, 2023, **33**, 2306060.

10 N. Kamaya, K. Homma, Y. Yamakawa, M. Hirayama, R. Kanno, M. Yonemura, T. Kamiyama, Y. Kato, S. Hama, K. Kawamoto and A. Mitsui, *Nat. Mater.*, 2011, **10**, 682–686.

11 C. Sun, J. Liu, Y. Gong, D. P. Wilkinson and J. Zhang, *Nano Energy*, 2017, **33**, 363–386.

12 X. Yu and W. Ren, *Nat. Commun.*, 2023, **14**, 3998.

13 Z. W. B. Iton and K. A. See, *Chem. Mater.*, 2022, **34**, 881–898.

14 Z. W. B. Iton, Z. Irving-Singh, S.-J. Hwang, A. Bhattacharya, S. Shaker, T. Das, R. J. Clément, W. A. Goddard, III and K. A. See, *J. Am. Chem. Soc.*, 2024, **146**, 24398–24414.

15 M. K. Sarango-Ramírez, M. Donoshita, Y. Yoshida, D.-W. Lim and H. Kitagawa, *Angew. Chem., Int. Ed.*, 2023, **62**, e202301284.

16 C. Yan, C. Lv, Y. Zhu, G. Chen, J. Sun and G. Yu, *Adv. Mater.*, 2017, **29**, 1703909.

17 X. Qian, L. Chen, L. Yin, Z. Liu, S. Pei, F. Li, G. Hou, S. Chen, L. Song, K. H. Thebo, H.-M. Cheng and W. Ren, *Science*, 2020, **370**, 596–600.

18 S. Acosta, H. J. Ojeda-Galván and M. Quintana, *Phys. Chem. Chem. Phys.*, 2023, **25**, 24264–24277.

19 L. Zhang, J. Yan, Z. Wang, T. Zhang, S. Song, M. Quintana and Y. Zhao, *Adv. Mater.*, 2025, e12998.

20 J. Wang, X. Zhang, Z. Yu, Y. Gao, Q. Lu, C. Ma, K. Liu, Q. Yuan and Y. Yang, *Natl. Sci. Rev.*, 2025, **12**, nwae482.

21 Y. Zhang, D. Chen, W. He, J. Tan, Y. Yang and Q. Yuan, *Adv. Mater. Technol.*, 2023, **8**, 2202014.

22 A. Esfandiar, B. Radha, F. C. Wang, Q. Yang, S. Hu, S. Garaj, R. R. Nair, A. K. Geim and K. Gopinadhan, *Science*, 2017, **358**, 511–513.

23 Y. Xue, Y. Xia, S. Yang, Y. Alsaid, K. Y. Fong, Y. Wang and X. Zhang, *Science*, 2021, **372**, 501–503.

24 J. Peng, Y. Liu, Y. Pan, J. Wu, Y. Su, Y. Guo, X. Wu, C. Wu and Y. Xie, *J. Am. Chem. Soc.*, 2020, **142**, 18645–18651.

25 J. Park, S. Bhoyate, Y.-H. Kim, Y.-M. Kim, Y. H. Lee, P. Conlin, K. Cho and W. Choi, *ACS Nano*, 2021, **15**, 12267–12275.

26 J. Abraham, K. S. Vasu, C. D. Williams, K. Gopinadhan, Y. Su, C. T. Cherian, J. Dix, E. Prestat, S. J. Haigh, I. V. Grigorieva, P. Carbone, A. K. Geim and R. R. Nair, *Nat. Nanotechnol.*, 2017, **12**, 546–550.

27 Y. Yang, X. Yang, L. Liang, Y. Gao, H. Cheng, X. Li, M. Zou, R. Ma, Q. Yuan and X. Duan, *Science*, 2019, **364**, 1057–1062.

28 Z. Dai, P. Jin, S. Yuan, J. Yang, K. V. Agrawal and H. Wang, *Nat. Commun.*, 2025, **16**, 4626.

29 Q. Zhao, S. Stalin, C.-Z. Zhao and L. A. Archer, *Nat. Rev. Mater.*, 2020, **5**, 229–252.

30 J. Shen, G. Liu, Y. Han and W. Jin, *Nat. Rev. Mater.*, 2021, **6**, 294–312.

31 T. Zhang, H. Bai, Y. Zhao, B. Ren, T. Wen, L. Chen, S. Song and S. Komarneni, *ACS Nano*, 2022, **16**, 4930–4939.

32 X. He, Y. Zhu and Y. Mo, *Nat. Commun.*, 2017, **8**, 15893.

33 D. Lei, Y. Wang, Q. Zhang, S. Wang, L. Jiang and Z. Zhang, *Nat. Commun.*, 2025, **16**, 754.

34 D. A. Köpfer, C. Song, T. Gruene, G. M. Sheldrick, U. Zachariae and B. L. de Groot, *Science*, 2014, **346**, 352–355.

35 B. J. Hinds, *Science*, 2021, **372**, 459–460.

36 X. Jiang, L. Zhang, Y. Miao, L. Chen, J. Liu, T. Zhang, S. Cheng, Y. Song and Y. Zhao, *Water Res.*, 2025, **276**, 123291.

37 S. Chang, J. Liu, J. Chen, Y. Zhang, Z. Wang, Z. Huang and B. Liu, *Small*, 2025, **21**, 2504191.

38 W. Wang, Y. Zhao, L. Chen, L. Zhang, T. Wen, Z. Wang and T. Zhang, *Chem. Eng. J.*, 2024, **500**, 156801.

39 J. Hu, X. Tang, Q. Dai, Z. Liu, H. Zhang, A. Zheng, Z. Yuan and X. Li, *Nat. Commun.*, 2021, **12**, 3409.

40 L. Zhang, Z. Wang, T. Zhang, X. Jiang, L. Chen, H. J. Ojeda-Galván, M. Quintana, S. Song, S. Komarneni and Y. Zhao, *ACS Mater. Lett.*, 2025, **7**, 2835–2843.

41 L. Zhong, S. Hu, X. Yang, M. Yang, T. Zhang, L. Chen, Y. Zhao and S. Song, *Colloids Surf., A*, 2021, **617**, 126364.

42 W. Yu, Z. Ge, K. Zhang, X. Liang, X. Ge, H. Wang, M. Li, X. Shen, Y. Xu, L. Wu and T. Xu, *Ind. Eng. Chem. Res.*, 2022, **61**, 4329–4338.

43 J. Hao, C. Bi, S. Li, S. Zhao, S. Yang, Y. Li and T. E, *Int. J. Biol. Macromol.*, 2025, **284**, 138160.

44 H. Wang, P. Wen, Y. Liu, S. Han, Z. Zhang, Y. Xu, M. Chen and X. Lin, *J. Am. Chem. Soc.*, 2025, **147**, 14554–14563.

45 Q. Zhang, Y. Ma, Y. Lu, L. Li, F. Wan, K. Zhang and J. Chen, *Nat. Commun.*, 2020, **11**, 4463.

46 Y. Okazaki, T. Taniuchi, G. Mogami, N. Matubayasi and M. Suzuki, *J. Phys. Chem. A*, 2014, **118**, 2922–2930.

47 M. Botta, S. Merk, R. J. Spranger, A. Senyshyn, V. Baran, V. Dyadkin, L. van Wüllen and T. F. Fässler, *Angew. Chem., Int. Ed.*, 2025, **64**, e202419381.

48 Z. Zhang, L. Liang, J. Feng, G. Hou and W. Ren, *Nat. Commun.*, 2024, **15**, 2706.

49 X. Zhou, Y. Huang, B. Wen, Z. Yang, Z. Hao, L. Li, S.-L. Chou and F. Li, *Proc. Natl. Acad. Sci. U. S. A.*, 2024, **121**, e2316914121.

50 Z. Lu, H. Yang, Y. Guo, H. Lin, P. Shan, S. Wu, P. He, Y. Yang, Q.-H. Yang and H. Zhou, *Nat. Commun.*, 2024, **15**, 3497.

51 M. Ding, H. Xu, W. Chen, Q. Kong, T. Lin, H. Tao, K. Zhang, Q. Liu, K. Zhang and Z. Xie, *J. Mater. Chem. A*, 2020, **8**, 22666–22673.

52 X. Yang, C. Li, P. Liu, Y. Zhai, I. Hussain, X. Sui, L. Gao and L. Jiang, *Chem. Mater.*, 2023, **35**, 7266–7272.

53 R. Guo, Y. Zhou, W. Wang, Y. Zhai, X. Liu, W. He, W. Ou, R. Ding, H.-L. Zhang, M. Wu, Z. Jiang and K.-G. Zhou, *Sci. Adv.*, 2025, **11**, eadr5374.

54 Z. Li, W. Wang, Y. Chen, C. Xiong, G. He, Y. Cao, H. Wu, M. D. Guiver and Z. Jiang, *J. Mater. Chem. A*, 2016, **4**, 2340–2348.

55 A. R. Koltonow and J. Huang, *Science*, 2016, **351**, 1395–1396.

56 J. Tang, Y. Wang, H. Yang, Q. Zhang, C. Wang, L. Li, Z. Zheng, Y. Jin, H. Wang, Y. Gu and T. Zuo, *Nat. Commun.*, 2024, **15**, 3649.

57 L. Cao, H. Wu, X. He, H. Geng, R. Zhang, M. Qiu, P. Yang, B. Shi, N. A. Khan and Z. Jiang, *J. Mater. Chem. A*, 2019, **7**, 25657–25664.